Chapter 3: Design of a Wide-Bandwidth Dual-Band Ingestible Antenna for Wireless Capsule Endoscopy

In this chapter, we present a wide-bandwidth dual wide-band ingestible antenna design for wireless capsule endoscopy (WCE) biotelemetry applications. The design process employs Characteristic Mode Analysis (CMA) and driven modal analysis. The effectiveness of the prototype antenna is afterward assessed through measurements using a tissue-equivalent phantom liquid model. We investigate the effects of antenna implantation depth and capsule shell thickness on its performance, providing insights into practical considerations. The proposed dual-band antenna demonstrates good performance in both the 1.4 GHz Wireless Medical Telemetry Services (WMTS) and 2.45 GHz Industrial, Scientific, and Medical (ISM) bands, exhibiting measured impedance bandwidths of 36% and 22%, respectively. The measured peak realized gains are -22.9 dBi and -25.3 dBi for the WMTS and ISM bands, respectively, with a compact footprint of 78.5 mm². To ensure health and safety and optimal performance, we evaluate the antenna's specific absorption rate (SAR) and link margin (LM). Additionally, we assess the performance of the proposed antenna in comparison with the state-of-the-art design for capsule antennas in WCE applications.*

*Part of this chapter have been published: Dubey, R., Singh, A., Srivastava, S. K., & Meshram, M. K. (2023). A dual wide-band ingestible antenna design for wireless capsule endoscopy. *AEU-International Journal of Electronics and Communications*, *172*, 154935.

3.1 Introduction

Wireless capsule endoscopy (WCE) is a non-invasive medical imaging technique that enables the examination of the gastrointestinal tract using a small, ingestible capsule equipped with a camera and an antenna. The capsule captures images of the interior of the gastrointestinal tract and wirelessly transmits them to a receiver outside the body [93]-[94]. The design and optimization of the antenna are crucial for WCE's performance, as it is responsible for transmitting data and images from the capsule to the receiver.

The current state-of-the-art in WCE primarily involves the use of single-band antennas operating at frequencies such as 2.4 GHz [39],[95], 1400 MHz [40], 915 MHz [41]-[44][51], and 433 MHz [44]-[46]. These single-band antennas can potentially cause interference with other wireless devices and may not offer sufficient bandwidth for high-resolution images. Additionally, the dynamic movement of the capsule within the human body makes establishing secure and stable communication links between the capsule and an external receiver challenging. To overcome these limitations, recent years have seen the proposal of dual-band [47]-[52], and multi-band [53],[103] antenna designs, including wide-band configurations [104].

However, these antenna designs often feature complex geometries and lack a fundamental understanding of the radiating structure. Notably, magnetic antennas, as discussed in [57], offer improved performance in lossy dielectrics compared to electric field antennas like dipoles [40],[41],[44],[95], planar inverted F-antennas [42][47][49], and patches [38][51]-[54]. This makes them a suitable choice for implanted applications subject to strict specific absorption rate (SAR) regulations. Traditional antenna design methods might struggle to address these challenges, potentially leading to suboptimal performance and reduced reliability of wireless communication in WCE systems.

Characteristic Mode Analysis (CMA) emerges as an effective approach for optimizing the antennas [9]-[98]. In this paper, we employ CMA to design a dual wide-band antenna for WCE. The proposed antenna operates across both Wireless Medical Telemetry Services (WMTS) and Industrial, Scientific, and Medical (ISM) bands (1.395-1.400 & 1.427-1.432 GHz and 2.400-2.4835 GHz), ensuring compliance with SAR regulations and enabling a reliable Link margin (LM) for wireless communication. The wide-bandwidth dual-band operation is achieved by harnessing the resonant properties of the characteristic modes (CMs), which can accommodate multiple frequency bands. Additionally, we explore the effects of antenna implantation depth and capsule shell thickness on the antenna's performance, providing valuable insights into practical considerations. We comprehensively evaluate the antenna's performance through simulations, measurements, and comparative analysis across diverse capsule endoscopy antenna designs, including single-band and multiple-band configurations. This includes a comparison with state-of-the-art designs, assessing our antenna's effectiveness within the specific WMTS and ISM frequency bands.

3.2 Antenna Design and Performance

The antenna design and device architecture are depicted in Fig. 3.1, which includes a top view (Fig.3. 1(a)), an isometric view (Fig. 3.1(b)), and a comprehensive exploded view (Fig. 3.1(c)). The antenna structure encompasses a folded metallic annular ring, a shorting pin, and a 50-Ω coaxial feed. As seen from the enlarged view, the folded metallic ring structure is a key feature of this design, which makes it unique from other designs, which is achieved by exploiting the resonant properties of the Characteristic modes (CMs). The ring structure, which acts as the radiating element, is made of a conductive metal and is folded in a specific pattern to achieve dual-band operation. The proposed antenna has a

compact size and it is designed to fit inside a capsule with dimensions of approximately 11 mm X 26 mm [95].

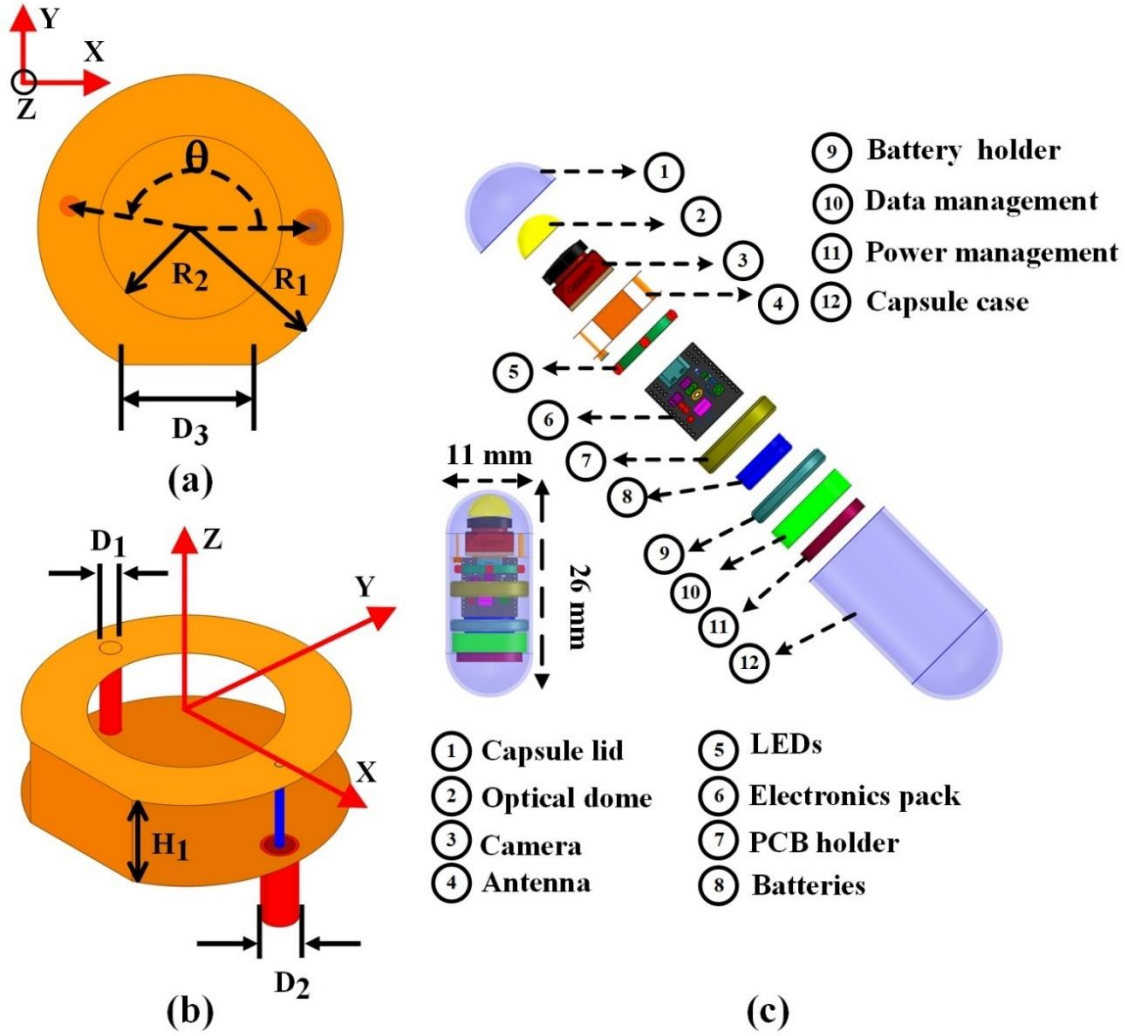

Fig. 3.1: (a) Top view of the antenna, (b) Isometric view of the antenna. (Physical dimension: D_1=0.68mm, D_2=2.38 mm, D_3=4.35 mm, H_1= 3.0 mm, R_1= 5.0 mm, R_2=3.0 mm,θ = 170°, and (c) Exploded view of device architecture.

3.2.1 Modal Analysis of the Antenna

To enhance the antenna's design optimization, the utility of CMA is paramount as an initial directive. The theoretical framework of characteristic modes was originally propounded by Garbacz and Turpin [96], with later re-evaluation by Harrington and Mautz in 1971 [97]. CM, being independent of excitation, hinge on the size of the conducting bodies [98]. This

intrinsic feature renders feasible the design of arbitrarily contoured antennas that align with prescribed radiation characteristics.

The underlying framework rests upon generalized eigenvalue equations defined as follows:

$$X(J_n) = \lambda_n R(J_n) \tag{3.1}$$

Where λ_n and J_n represent Eigenvalues and Eigen currents, while *R* and *X* denote the real and imaginary components of the impedance operator. Resonance is identified when λ_n equals zero. Negative values signify capacitive tendencies, whereas positive values connote inductive characteristics. For a more comprehensive grasp of resonance in distinct modes, the modal significance value (MS), representing the normalized amplitude of current modes [63], emerges as an illuminating metric. It is expressed as follows:

$$\text{MS} = \left| \frac{1}{1+j\lambda_n} \right| \tag{3.2}$$

A mode attains optimal radiation when its MS value equates to unity. The width of the MS value around its maximum point indicates the operating bandwidth of the conducting object. Since modal analysis doesn't consider antenna excitation, the radiator can be analysed devoid of any substrate and phantom model.

The radiating structure of the dual-band antenna for wireless capsule endoscopy is designed using CMA through CST Microwave Studio 2021. The design process of the antenna involved an evolution from Case-I to Case-V, as shown in Fig.3. 2. The CMA reveals that the antenna structure has two dominant modes, Mode 1 and Mode 3. The modal currents J_1 and J_3, as shown in Figs. 3.2(a) to 3.2(e) represent the longitudinal and higher-order modal current distribution, respectively, and are crucial for the design of the dual-band antenna. The longitudinal current (J_1) is associated with the low-frequency band and creates a uniform current distribution along the length of the antenna element. The higher-order modal current (J_3) is associated with the high-frequency band and creates a current

distribution in the plane. As the antenna structure evolved from Case-I to Case-V, shifts in MS are observed, as demonstrated in Fig. 3.3. In Case-I, a conventional metallic rectangular strip with dimension of 23 mm x 10 mm is chosen as the antenna type. In Case-II, the rectangular metallic strip is transformed into a dumbbell-shaped structure, elongating the current path and decreasing the MS of Mode 1 and Mode 3, as shown in Fig. 3.3(a), and Fig. 3.3(b), respectively.

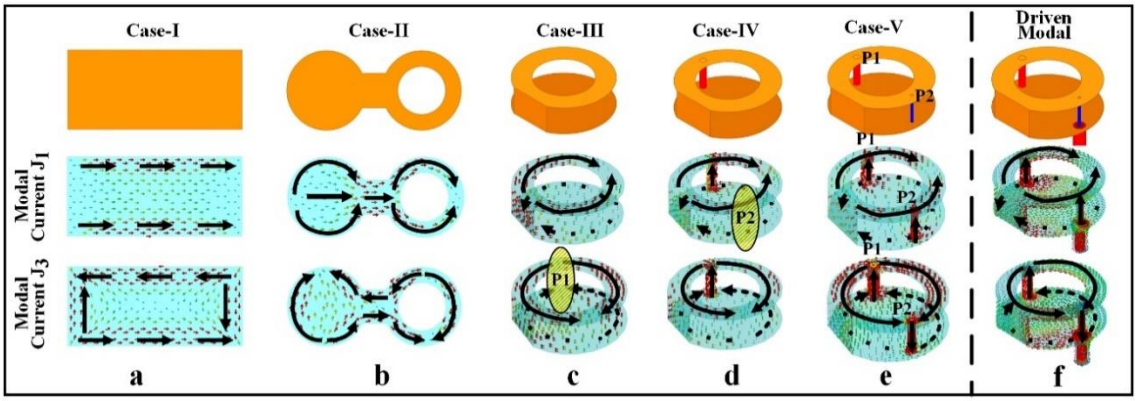

Fig. 3.2: Antenna evolution using CMA

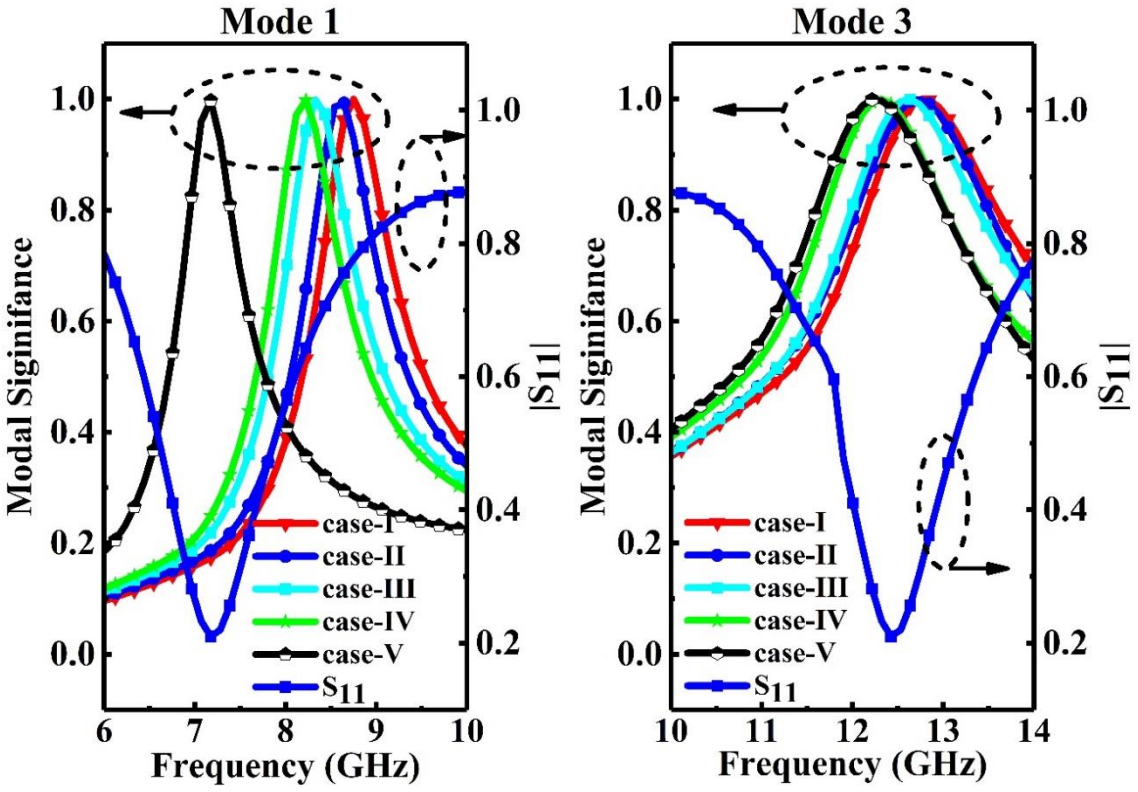

Fig. 3.3: Modal significances and $|S_{11}|$ of (a) Mode-1, and (b) Mode-3.

As the antenna structure evolved from Case-II to Case-III, the folding of the dumbbell shape further decreased the MS of Mode 1 and Mode 3. The folding of the antenna has a decreasing effect on the MS due to an increase in inductance. The folding of the dumbbell shape also allowed the antenna to fit into the upper part of the dome of the capsule. In Case-IV, a metal pin is introduced at position P1, causing a shift in the MS at a higher frequency for mode 3. The introduction of the metal pin increases the inductance of the antenna, due to which MS decreases. Finally, in Case-V, a second pin is introduced at position P2 as a feed, causing a shift in the MS of Mode1, since it now acts as a dipole, and a small shift in the MS of Mode3, since it now acts as a loop. To verify the final antenna structure in Case-V acts as desired for the dominant modes, Mode 1 and Mode 3, as predicted by the CMA in Fig. 3.2(e), a second pin at position P2 is replaced with coaxial feed, as shown in Fig. 3.2(f). The results of the driven-model analysis are then compared with the modal significance and $|S_{11}|$, as shown in Fig.3.3, to confirm the accuracy of the CMA predictions and the performance of the antenna structure in Case-V. In Fig. 3.2, the surface current distributions for Mode 1 and Mode 3 are depicted. These modes correspond to dipole and loop-type configurations (case-V). It is noteworthy that the source excites these two modes simultaneously, with Mode 1 exhibiting a maximum surface current while Mode 3 displays a minimum surface current. The strategic placement of the source at position P2 is found to be optimal for exciting all the desired CMs. The spatial separation between these two dominant modes is notably significant. This spatial divergence serves to mitigate interactions between the modes, ultimately contributing to the broadening of the antenna's impedance bandwidth within their respective modal significance spectra (MS).

3.2.2 S-parameter in Different Phantom

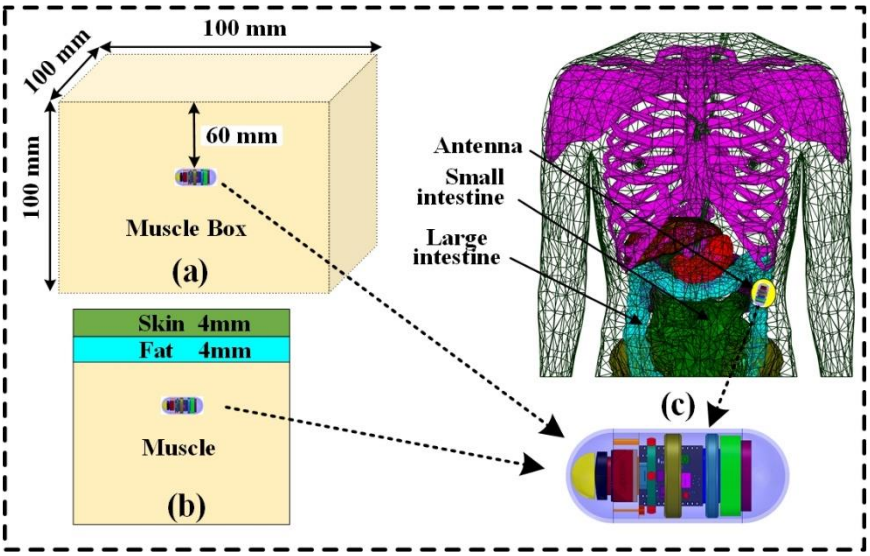

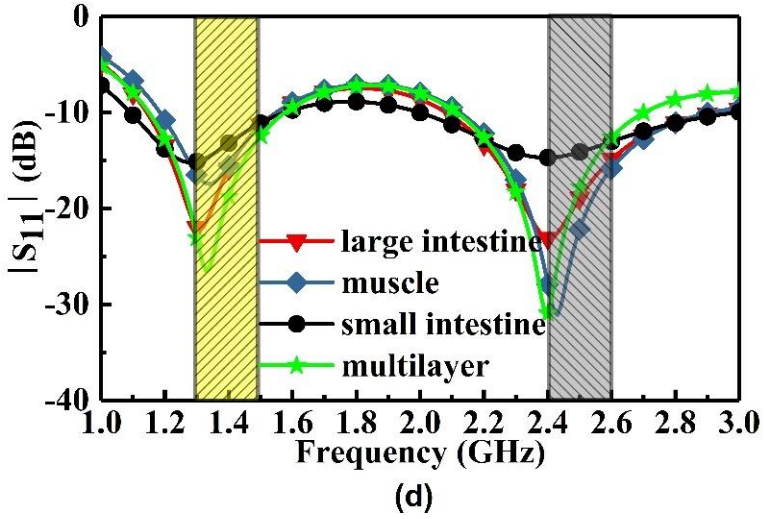

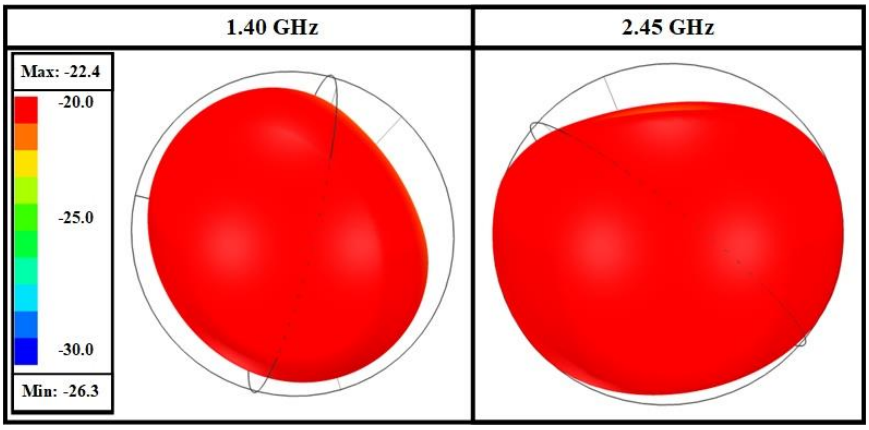

Fig. 3.4: Simulation models. (a) One-layer muscle phantom, (b) multilayer tissue model, (c) Realistic human model, (d) Comparison $|S_{11}|$ of proposed antenna in different simulation setups and (e) simulated capsule antenna's 3-D radiation pattern.

Initially, the resonance of the antenna was obtained through CMA in a free-space environment. This allowed us to evaluate the antenna's performance in a controlled setting and optimize its design for desired characteristics. However, to effectively use the antenna in a WCE system, it is necessary to consider the impact of the body's conductivity and permittivity on its performance.

Table 3.1: Electrical properties of the body tissues at the dual-band [101].

Electrical properties	**Relative Permittivity ε_r**		**Conductivity σ (S/m)**	
Frequency (GHz)	1.4 GHz	2.45 GHz	1.4 GHz	2.45 GHz
Skin	44.62	38.00	1.04	1.46
Fat	5.39	5.28	0.06	0.10
Muscle	54.11	54.41	1.14	1.88
Small Intestine	57.10	54.42	1.53	3.17
Large Intestine (Colon)	56.12	53.87	1.33	2.03

Table 3.2: Impedance bandwidth and peak realized gain at different simulation environments.

Implanted Scenario	**Bandwidth (MHz)**		**Peak Realized Gain (dBi)**	
	WMTS	**ISM**	**WMTS**	**ISM**
One-layer Muscle Phantom	370	790	-22.4	-26.5
Multilayer Muscle Phantom	430	580	-29.7	-32.9
Small Intestine	490	990	-28.1	-32.3
Large Intestine (Colon)	410	850	-24.5	-28.4

In a lossy medium, the antenna size is directly proportional to the operating wavelength, which impacts its performance. Thus, we incorporated the frequency-dependent dielectric

properties of muscle tissue to account for this effect. We used the equation $f_r = c/(2l_g\sqrt{\varepsilon_{eff}})$, to estimate the shift in frequency, where $c = 3 \times 10^8 m/s$, ε_{eff} is the effective permittivity of the medium, and l_g is the length of the antenna. To accurately assess the antenna's performance, we utilized three distinct models in our simulations: a single-layer homogeneous muscle tissue model [3] with dimensions of 100 mm x 100mm x 100 mm and an implantation depth of 60 mm, a multilayer model and a realistic human anatomical model (as shown in Fig. 3.4(a)). The frequency-dependent electrical characteristics of distinct body tissues at the dual-band frequencies of 1.4 GHz and 2.45 GHz are depicted in Table-3.1. The simulation results for the proposed antenna design, illustrated in Fig. 3.4(d), show a comparison of the $|S_{11}|$ values obtained from each model. $|S_{11}|$ represents the reflection coefficient, which indicates how well the antenna is matched to the transmission line. Fig. 3.4(e) presents the simulation results of the proposed capsule antenna's 3-D radiation pattern. It is observed that the antenna achieves maximum and minimum realized gains of -22.4 dBi and -26.3 dBi, respectively, across both the WMTS and ISM bands. This results in a gain variation of 3.9 dB, clearly indicating the quasi-isotropic radiation pattern demonstrated by the proposed antenna configuration. It is observed that the $|S_{11}|$ is well below -10 dB for the WMTS and ISM bands, making it suitable for WCE. The impedance bandwidth and peak realized gain across diverse simulation scenarios are presented in Table3.2. The data in the table reveals that the antenna showcases a substantial impedance bandwidth across a range of implanted scenarios. Furthermore, the observed peak realized gains in different tissue models conform to the acceptable parameters for WCE communication systems.

3.2.3 Effect of H_1

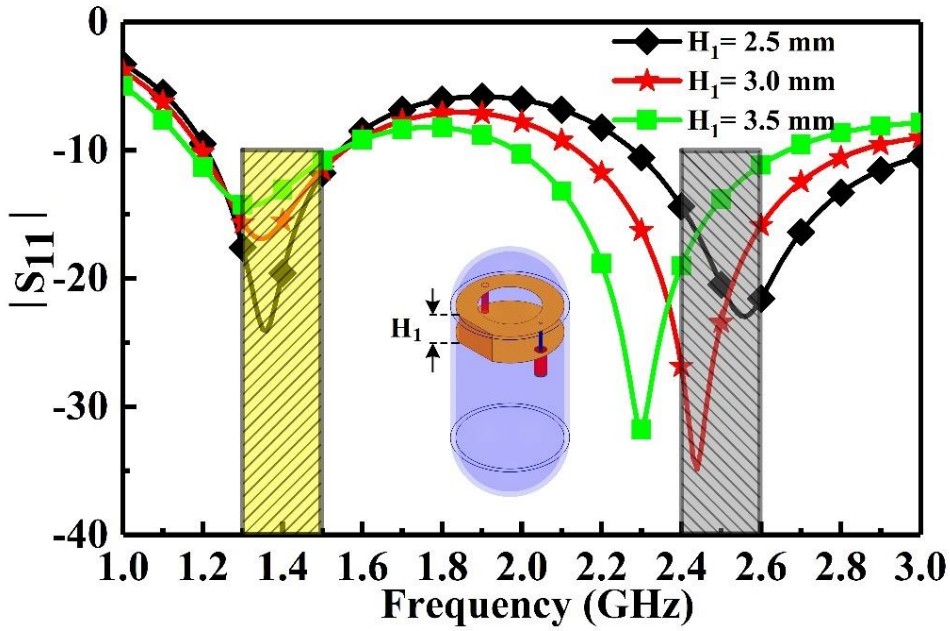

Fig. 3.5: Variation of the antenna reflection coefficient $|S_{11}|$ with H_1

Fig. 3.5 illustrates the $|S_{11}|$ parameters of the antenna for varying H_1 values at 2.5, 3.0, and 3.5 mm while keeping all other physical parameters constant. Notably, it becomes evident that alterations in H_1 have a differential impact on the antenna's performance in different frequency bands. Observations reveal those variations in H_1 influence the lower frequency WMTS band to a lesser extent, while significantly affecting the higher frequency ISM band. Specifically, as H_1 increases from 2.5 mm to 3.0 mm and 3.5 mm, a noticeable leftward shift occurs in the resonance frequency of the higher frequency ISM band. This phenomenon can be attributed to the increased electrical length introduced by altering H_1. For achieving optimal impedance bandwidth matching in both the WMTS and ISM bands, we should set H_1 to 3.0 mm.

3.2.4 Effect of Antenna Implantation Depth

The impact of the proposed antenna on implantation depth (D_t) in a homogeneous muscle phantom for wireless capsule endoscopy applications is being investigated. Three distinct

implantation depths are being examined: Dt = 40, 60, and 80 mm. The $|S_{11}|$, a critical performance metric, is being thoroughly assessed under these varying depths. Fig.3.6 is showing the $|S_{11}|$ of the antenna under various implantation depths. The $|S_{11}|$ parameter demonstrates good resilience to changes in implantation depth, manifesting a negligible frequency shift of less than 0.2%. The slight shift to a higher frequency with increasing implant depth is due to the fact that the dielectric constant of human tissue decreases with frequency. This negligible shift underscores the antenna's robustness and adaptability for WCE applications, ensuring reliable wireless connectivity throughout the capsule's traversal within the gastrointestinal tract. The observed consistency highlights the antenna's potential to function effectively at diverse tissue depths.

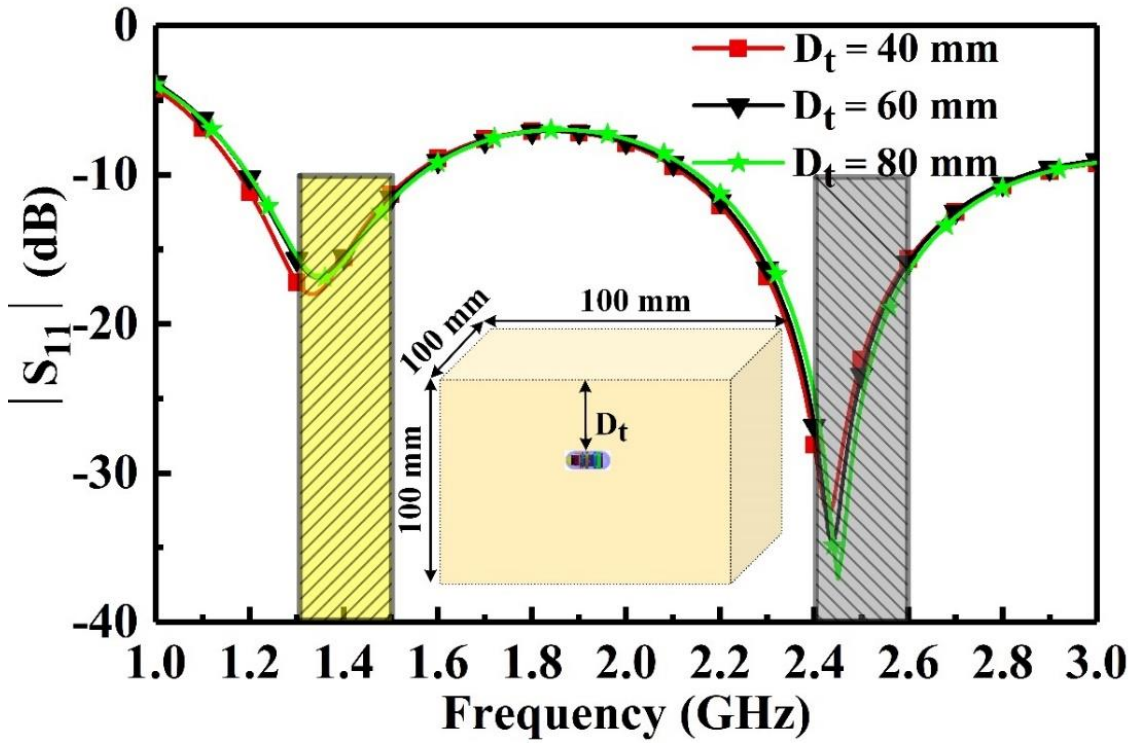

Fig. 3.6: Variation of the antenna reflection coefficient $|S_{11}|$ with different implantation depths.

3.2.5 Effect of Capsule shell thickness

In the exploration of capsule shell thickness's influence on the proposed antenna, we compare the effects of three capsule shell thicknesses: t = 0.40, 0.50, and 0.60 mm, on the antenna's $|S_{11}|$. The capsule shell comprises polymethylmethacrylate (PMMA), a biocompatible material. In Fig.3.7, the relationship between the antenna's $|S_{11}|$ and frequency is depicted for different capsule shell thicknesses. Analysing the antenna's $|S_{11}|$ reveals its minimal sensitivity to changes in capsule shell thickness, with a slight shift towards higher frequencies being observed. This behaviour underscores the limited impact of the capsule shell on the antenna's $|S_{11}|$. Due to brevity, we omit presenting the radiation performance impact, attributed to its very minimal influence. The consistent behaviour of the antenna's $|S_{11}|$ across distinct capsule shell thicknesses underscores its robustness in WCE.

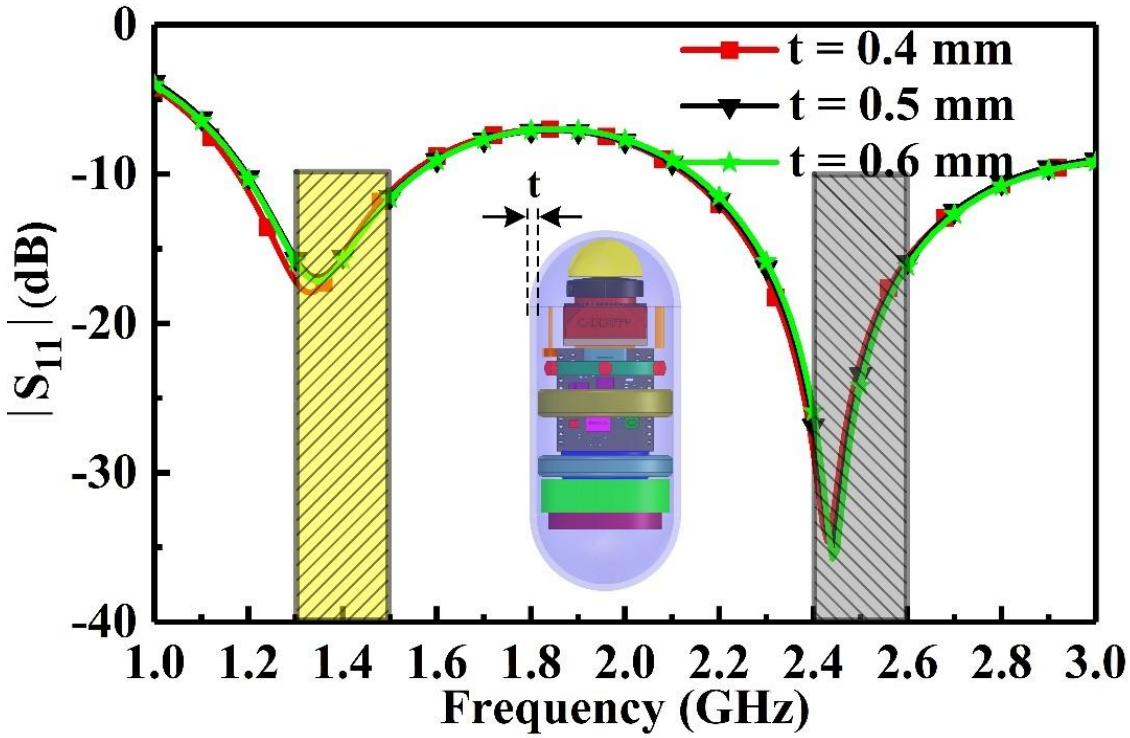

Fig. 3.7: Variations in the antenna $|S_{11}|$ with distinct capsule shell thicknesses.

3.2.6 Equivalent Circuit Analysis

To gain a comprehensive understanding of the working principle of the proposed antenna, we derived its equivalent circuit, as depicted in Fig. 3.8(b). We also analysed the variation of the antenna's input impedance, which is represented on a Smith chart in Fig. 3.8(a). This meticulous investigation revealed distinct impedance characteristics at different resonant frequencies. At the first resonance (approximately 1.4 GHz), the impedance manifested a parallel configuration featuring components Rp_1, Lp_1, and Cp_1. Below this resonance, the impedance displayed inductive behavior, while above it, it exhibited capacitive characteristics. The second resonance (around 1.71 GHz) exhibited a series-type impedance, characterized by components Rs_1, Ls_1, and Cs_1. Below this resonance, the impedance was capacitive, whereas above it, it demonstrated inductive behavior. The third resonance (around 2.45 GHz) returned to a parallel-type impedance, incorporating components Rp_2, Lp_2, and Cp_2. Below this resonance, the impedance was inductive, while above it, it became capacitive. The inductance L_f represented the coaxial cable, while the resistances Rp_1, Rs_1, and Rp_2 arose from losses in the biomedical environment. Circuit parameters were extracted using ADS and subsequently compared with results obtained from full-wave simulation (HFSS) and circuit simulation, as shown in Fig. 3.8(c) and 3.8(d), respectively, demonstrating good agreement at both frequency bands.

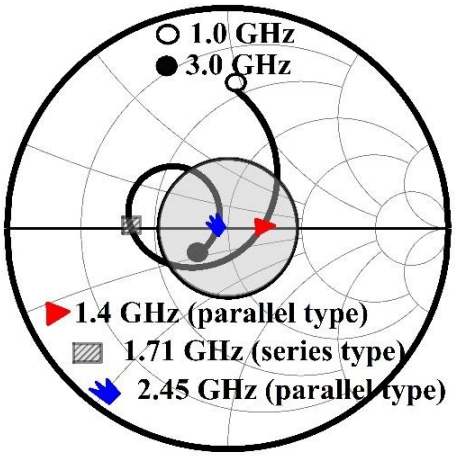

(a)

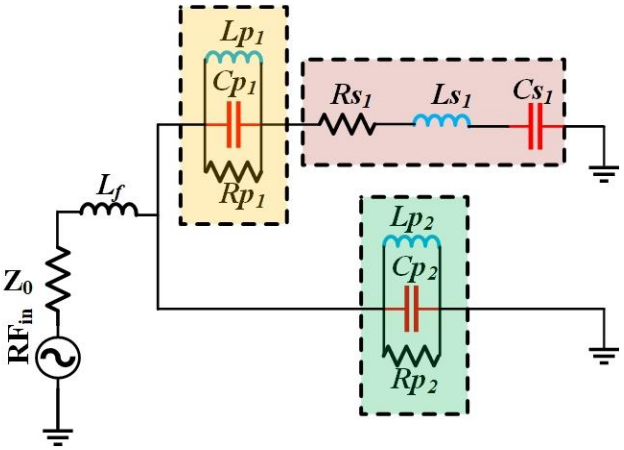

(b)

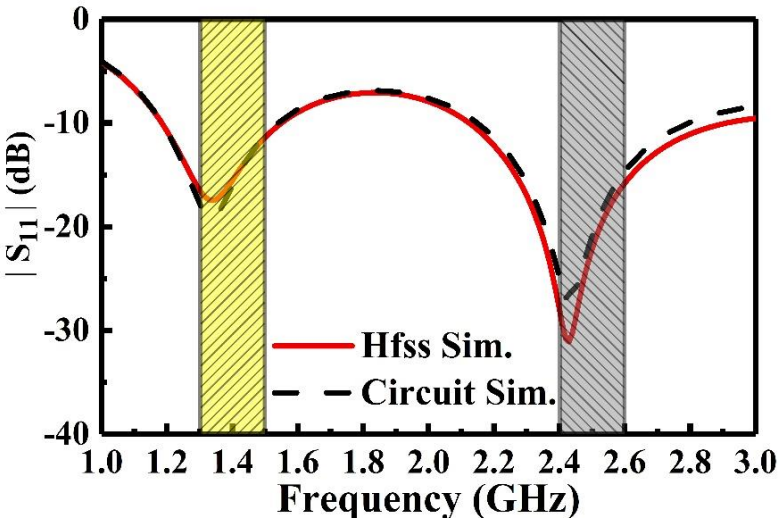

(c)

Parameters	
L_f	0.43 nH
Rp_1	59.72 ohm
Lp_1	0.87 nH
Cp_1	5.31 pF
Rp_2	131.16 ohm
Lp_2	3.48 nH
Cp_2	1.30 pF
Rs_1	20.19 ohm
Ls_1	2.88 nH
Cs_1	1.83 pF

(d)

Fig. 3.8: (a) Smith chart display of impedance (b) Equivalent circuit of the proposed antenna (c) compare $|S_{11}|$ full wave simulation and circuit simulation and (d) corresponding lumped elements values.

3.2.7 Effect of Electronic Components

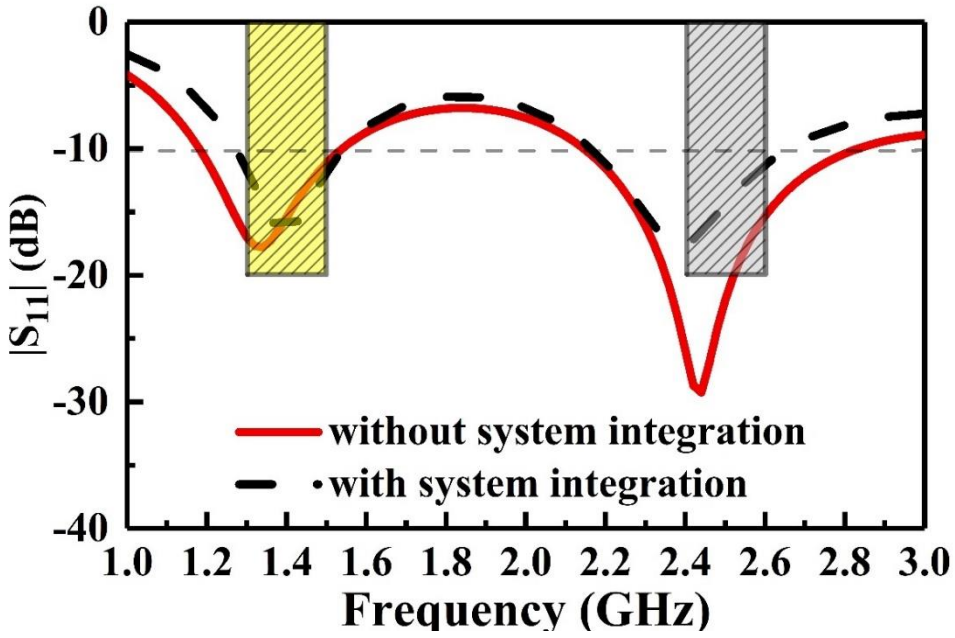

(a)

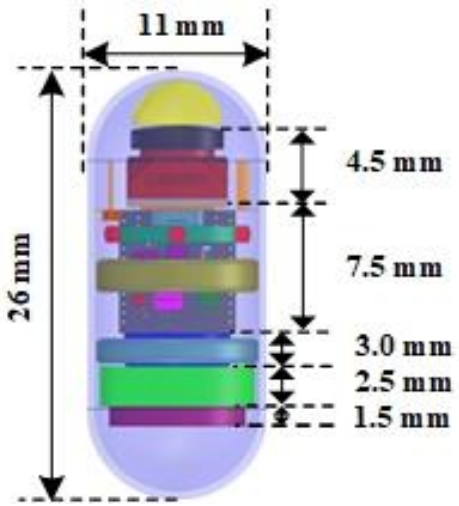

(b)

Fig. 3.9: (a) simulated $|S_{11}|$ of the proposed antenna in WCE system model, and **(b)** geometrical structure of WCE system model.

In a practical deployment, the WCE system model, depicted in Fig. 3.9(b), encompasses diverse electronic components. The implantable antenna is connected to a transceiver, which is an electronic pack modeled employing a combination of perfect electric conductor (PEC) and dielectric materials. The battery, with a 3 mm height is represented as a PEC.

Moreover, an optical dome with an arc at the top is modeled using polyvinyl chloride (PVC), while the power management unit is represented as a PEC. Other components within the system are modeled using PECs. The performance evaluation of the proposed antenna was conducted using simulated results obtained in a homogeneous muscle phantom, as illustrated in Fig. 3.9(a), by analysing the $|S_{11}|$ parameter with and without the WCE system. The $|S_{11}|$ value exhibits variation in response to the presence of the WCE system across both the WMTS and ISM bands. However, the performance of the proposed antenna effectively covers both frequency bands. These outcomes substantiate the strong robustness of the proposed antenna and its suitability for seamless integration into the WCE system.

3.2.8 Specific Absorption Rate Evaluation

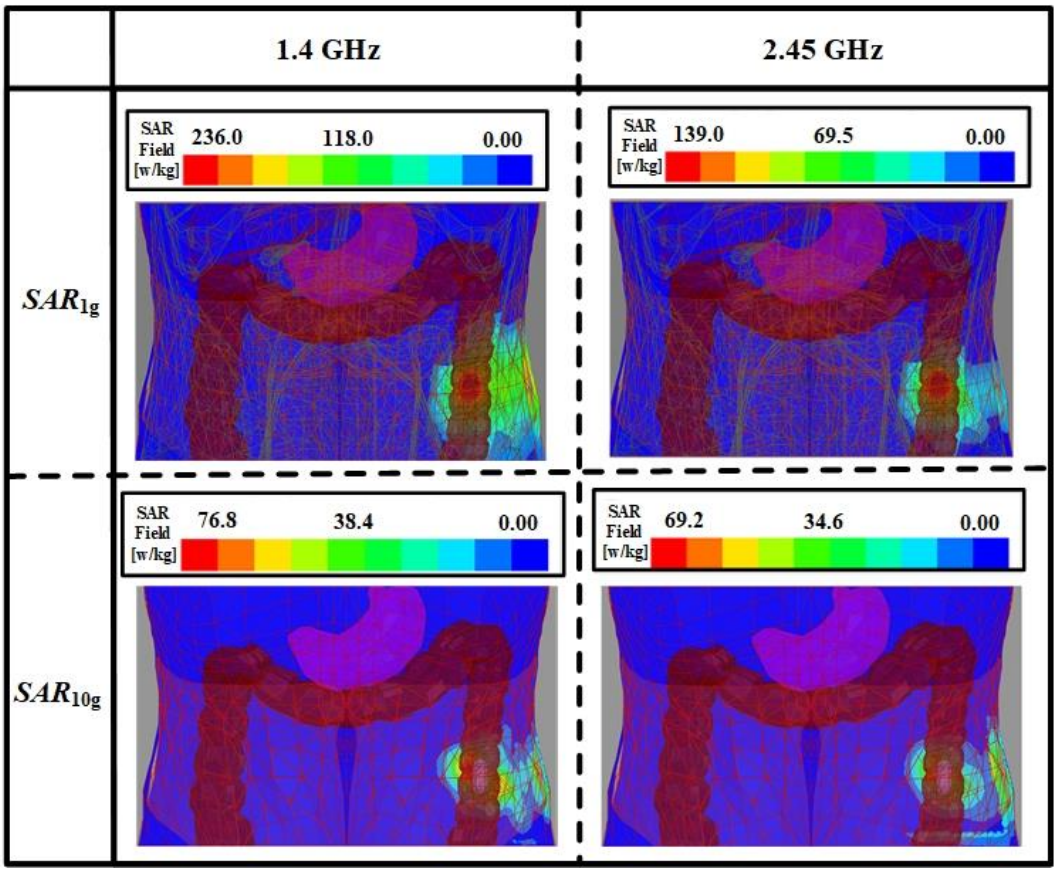

Fig. 3.10: Simulated average SAR distribution of the proposed antenna in human torso phantom model.

The evaluation of Specific absorption rate (SAR) is crucial for ensuring the safety and efficacy of the suggested dual-band antenna for WCE. SAR quantifies the rate at which body tissues absorb electromagnetic energy from the antenna's radiation. Fig.3.10 shows the simulated SAR distribution of the proposed antenna within a human torso phantom when the antenna delivers 1 W of power. The 1g SAR values for the proposed antenna were found to be 236 W/kg and 139 W/kg at the WMTS and ISM bands, respectively, for an input power of 1W. To ensure compliance with safety standards, the input power levels were maintained below 6.7 mW and 11.51 mW for the WMTS and ISM bands, respectively, in accordance with the IEEE C95.3-2021 standard [99]. Additionally, the 10g

Table 3.3: Simulated average SAR values (input power = 1 W) and calculated maximum input power at two typical frequencies

Frequency (GHz)	1-g Avg SAR (W/kg)	Max. input power (mW)	10-g Avg SAR (W/kg)	Max. input power (mW)
1.4	236	6.7	76.8	26.0
2.45	139	11.51	69.2	28.9

SAR values were simulated at 76.8 W/kg and 69.2 W/kg for the WMTS and ISM bands, respectively, at an input power of 1W. To meet safety guidelines outlined in the IEEE C95.1-2019 standard [65], the input power levels were kept below 26.2 mW and 28.9 mW for the WMTS and ISM bands, respectively. The lower SAR values at the ISM band can be attributed to the use of magnetic antennas, as reported in [57]. The detailed average SAR and the maximum allowable input power for 1g and 10g of tissue are shown in Table3. 3 for the proposed antenna at the WMTS and ISM bands.

3.2.9 Link Budget Analysis

To ensure a reliable biological telemetry link, a comprehensive link margin analysis was performed for the proposed dual wide-band implantable antenna. This analysis evaluated the communication link's performance, assessing the difference between the available received power and the required power at the receiver, as illustrated in Fig. 3.11, which presents the schematic setup for the link-budget analysis. The input power to the capsule-type antenna was constrained at −16 dBm (25 μW).

The link margin (dB) is derived through the subsequent equations:

$$Link\ margin(dB) = Link\ C/N_0 - Required\ C/N_0 \tag{3.3}$$

where, the Link C/N_0 (Carrier-to-Noise Ratio) represents the signal-to-noise ratio at the receiver, and the Required C/N_0 represents the minimum signal-to-noise ratio required for proper signal reception.

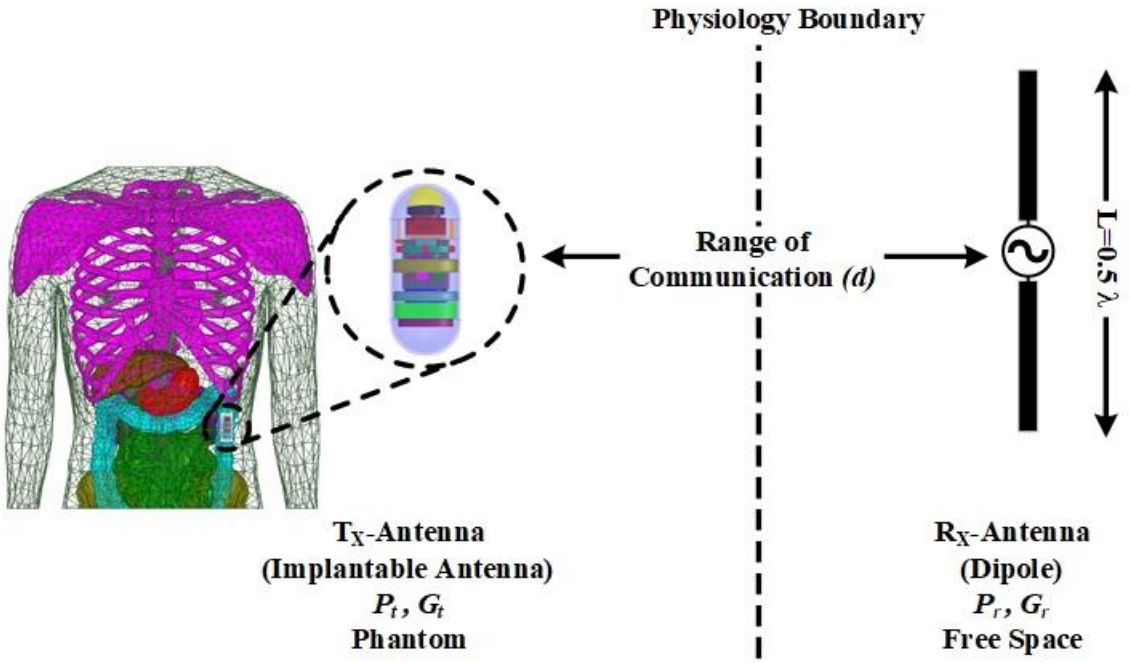

Fig. 3.11: Schematic setup for link-budget analysis

$$Link\ C/N_0 = P_t - L^t_{feed} - G_t - L_f - L_a + G_r - L^r_{feed} - N_0\ (\text{dB/Hz}) \tag{3.4}$$

$$Required\ C/N_0 = {}^{E_b}/_{N_0} + 10\log_{10}(B_r) + G_c(dB) + G_d(\text{dB}) \tag{3.5}$$

Table 3.4: Link budget parameters for the proposed dual-band antenna [42][44].

Transmission	Value
Frequency f (GHz)	1.40 / 2.45
Tx power P_t [W]	100×10^{-6}
Tx power P_t [dBW]	-40.00
Feeding loss L^t_{ffeed} [dB]	1.00
Tx antenna gain G_t [dBi]	-22.9 / -25.3
EIRP [dBw]	-48.9 / -51.3
Propagation	
Free space loss L_a [dB]	0.5
Path loss L_p [dB]	Distance dependent
Path loss exponent γ	1.5
Shadowing effect S_e (dB)	4
Receiver	
Rx antenna gain G_r [dBi]	2.15
Feeding loss L^r_{feed} [dB]	1.00
Ambient temperature T_0 [K]	293.0
Receiver – NF [dB]	3.5
Boltzmann constant k	1.38×10^{-23}
Noise power density N_0 [dB / Hz]	-203.5
Signal Quality	
Bit rate B_r [kbps]	100,250 1000
E_b/N_0 (ideal PSK) [dB]	9.6
Coding gain G_c [dB]	0
Fixing deterioration G_d [dB]	2.5

where P_t stands for transmitted power, G_t and G_r signify gains of the transmitting (capsule antenna) and received (dipole antenna) antennas, L^t_{feed} and L^r_{feed} depict losses in transmitted and received antenna feed systems, and L_p and N_0 denote free-space path loss at distance d between implanted transmitting (Tx) and receiving (Rx) antennas, as well as noise power density. The path loss, designated as L_p, encompasses diverse parameters, notably the path-loss exponent (γ), indicative of the rate at which received power attenuates with distance, along with the shadowing effect (S_e). Path-loss exponent(γ) values below two are frequently

observed in indoor propagation scenarios characterized by a direct line-of-sight (LOS) between the transmitter and receiver [68]. In indoor settings characterized by reflections, diffraction, and the scattering of electromagnetic waves, the transmitted signal follows multiple propagation paths to reach the receiver.

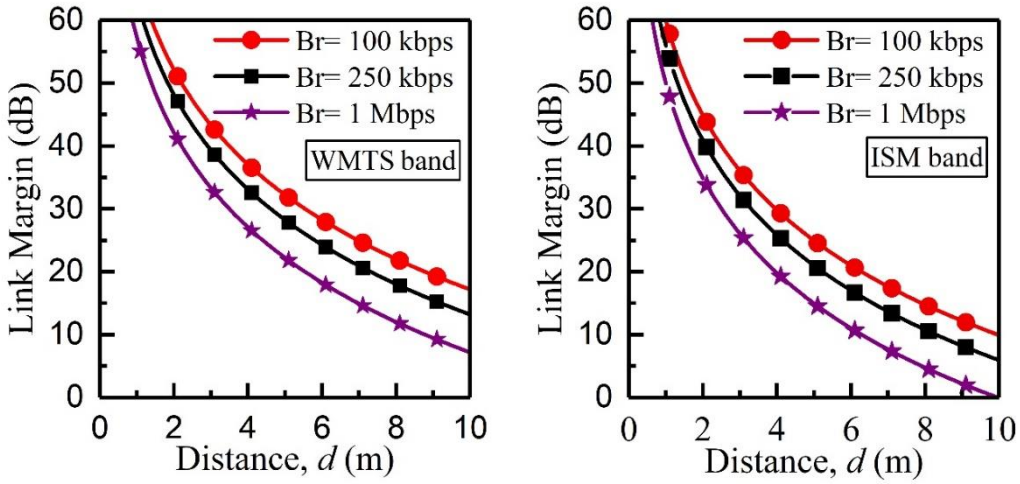

Fig. 3.12: Link margin versus distance for different data rate at (a) 1.4 GHz, and (b) 2.45 GHz.

These can be calculated as follows:

$$L_p = 10\log_{10}(\tfrac{4\pi d}{\lambda})^2 + 10\Upsilon\log_{10}(\tfrac{d}{d_0}) + S_e \text{ (dB)} \tag{3.6}$$

$$N_0 = 10\log_{10}(k) + 10\log_{10}(T_i) \text{ (dB/Hz)} \tag{3.7}$$

$$T_i = T_0(\text{NF} - 1) \text{ } (K) \tag{3.8}$$

Utilizing Table 3.4 parameters, link margin was computed. The transmission capsule antenna had gains of −22.9 dBi and -25.3 dBi at 1.4 GHz and 2.45 GHz, respectively. Fig. 3.12 shows the link margin versus distance for diverse bit rates at these frequencies, involving the proposed capsule antenna and external antenna. At a communication distance of 10 m and a frequency of 2.45 GHz, our analysis reveals impressive communication link margins for various bit rates. With margins exceeding 9.92 dB, 5.94 dB, and 0.01dB at bit

rates of 100 kbps, 250 kbps, and 1 Mbps, respectively, this implantable antenna demonstrates its capability to facilitate seamless data transmission. Likewise, at 1.4 GHz, the communication link margin continues to impress, surpassing 17.18 dB, 13.20dB, and 7.18dB for the corresponding bit rates of 100 kbps, 250 kbps, and 1 Mbps, respectively. These results underscore the antenna's reliability and efficiency in ensuring stable wireless communication within the allowable power range. Therefore, a reliable wireless communication link can be formed within the permissible input power range.

3.3 Measurement and Discussion

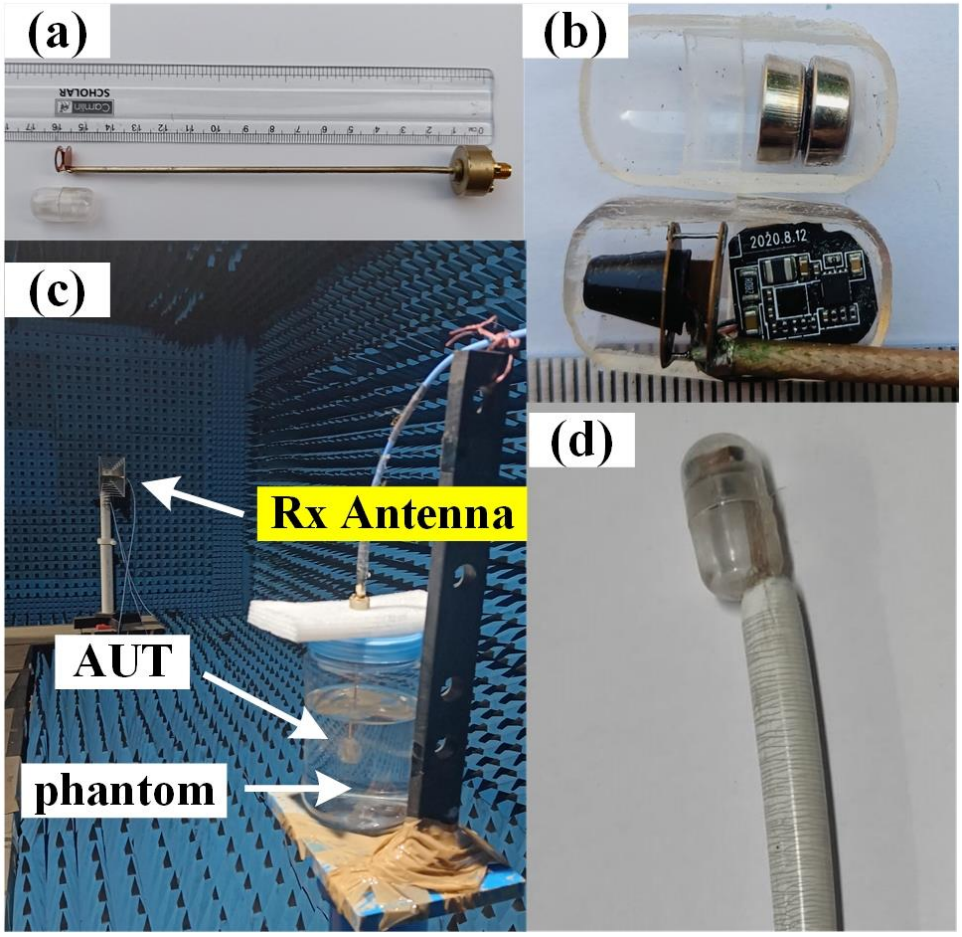

Fig. 3.13: Fabricated capsule antenna. (a) Decomposed capsule antenna. (b) Capsule device with dummy electronic components. (c) Measurement setup, and (d) Cable enclosed by vacuum shell.

In order to validate and evaluate the proposed dual-band antenna for WCE, the fabricated prototype is Measured. Fig3.13(a) and 3.13(b) show the decomposed and capsule device with dummy electronic components, while Fig. 3.13(c) depicts the measurement setup, and Fig. 3.13(d) shows the cable enclosed by vacuum shell [102]. The beaker phantom does not replicate the size or composition of a human torso but adheres to European Telecommunications Standards Institute (ETSI) guidelines for homogeneous liquid phantoms with muscle-like dielectric properties. This setup provides a controlled environment for initial antenna performance studies in a dielectric medium, facilitating the transition to more complex human models. Ethical considerations preclude the use of human torsos. The measurement are conducted inside a human equivalent liquid phantom using the Anritsu MS2038C vector network analyzer (VNA). The phantom is prepared using a recipe of 53% sugar, 47% deionized water, and 5.5g agarose, as described in [46]. The combined effects of tissue attenuation at the phantom, free space loss, and cable loss contribute to a total attenuation of approximately -70 to -80 dBm. Given the Anritsu MS2038C VNA's noise floor of -100 to -120 dBm/Hz, the received signal strength will be well above the noise floor by at least 20 dB. This ensures sufficient dynamic range for reliable radiation pattern measurements in the anechoic chamber. The measured reflection coefficient and realized gain of the proposed antenna are being compared with simulated results, as depicted in Fig. 3.14(a). The simulated impedance bandwidth of 26% (1.56-1.2 GHz) and 29% (2.85-2.14 GHz) whereas, the measured impedance bandwidth of 36% (1.61-1.1 GHz) and 22% (2.76-2.22 GHz) are observed for WMTS and ISM bands, respectively. Further, the simulated realized gain of -22.4 dBi and -26.5 dBi; and the measured realized gain of -22.9 dBi and -25.3 dBi are observed for WMTS and ISM bands, respectively. The measurement results demonstrate that the dual-band antenna designed for WCE exhibits good impedance matching and performance across both operating bands.

Fig. 3.14(b) presents a comparison between simulated and measured radiation patterns of the proposed antenna on the principal planes (XZ and XY) at 1.4 GHz and 2.45 GHz frequencies. Notably, the radiation pattern exhibited by the antenna is nearly symmetrical in both the XY and XZ planes for both frequencies. This characteristic is particularly advantageous for WCE applications, as it ensures consistent and comprehensive signal coverage, enhancing the antenna's suitability for medical imaging within the gastrointestinal tract. The simulated and measured results agree, as evidenced by the match observed in the result curves, although slight discrepancies between them can be attributed to minor variations in the electrical properties of the human-equivalent liquid phantom employed in the measurements, unexpected fabrication tolerances, and solder roughness. In addition, the performance of the antenna is compared to other antennas in the literature using a variety of parameters, as summarized in Table 3.5. The proposed antenna design provides a commendable harmony between size and performance, highlighting an impressive dual wide-band impedance bandwidth feature, alongside exceptional outcomes concerning SAR and gain.

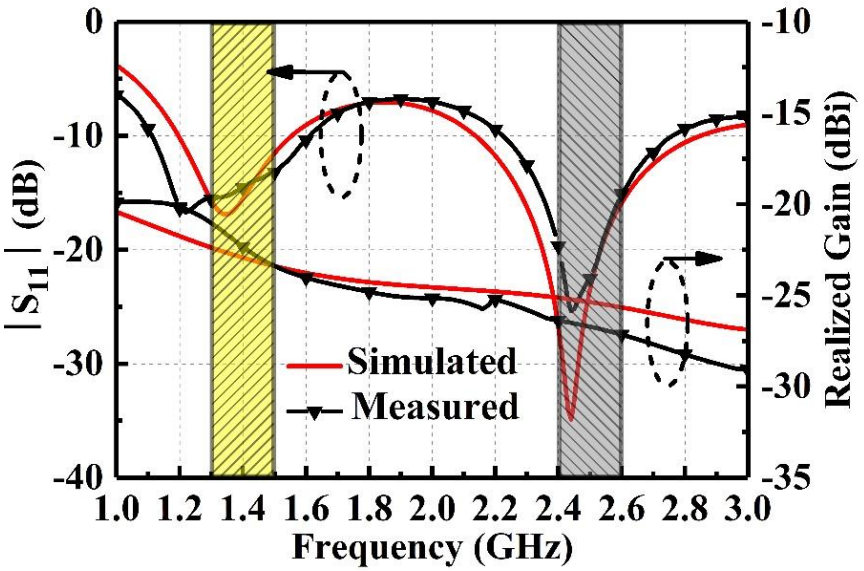

(a)

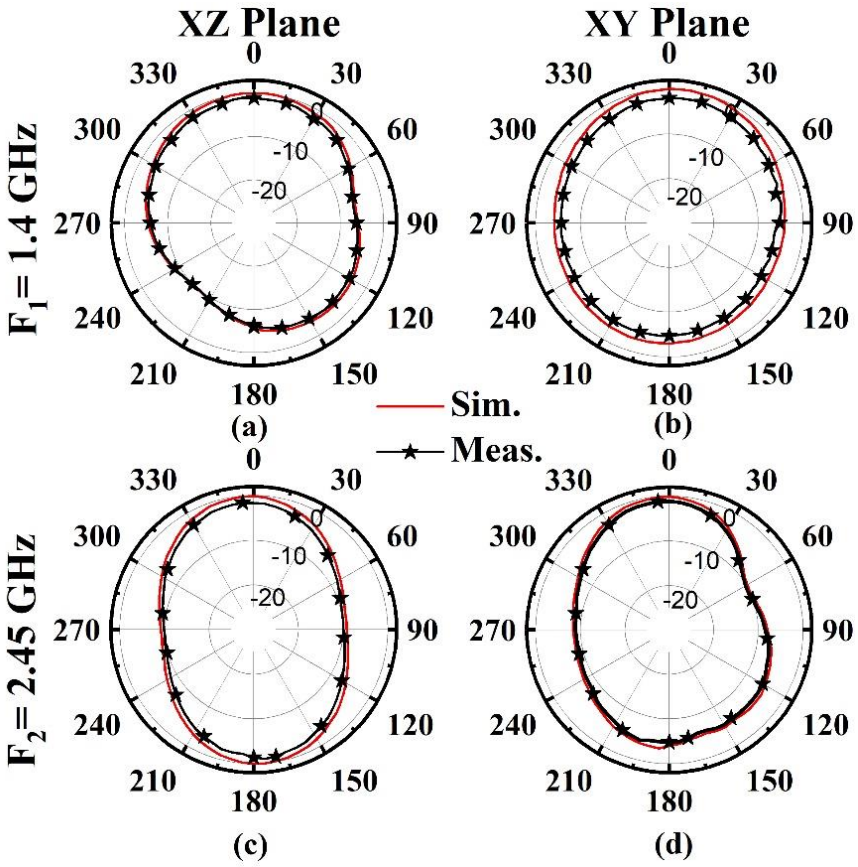

(b)

Fig. 3.14: Simulated and measured antenna results (a) Reflection coefficient frequency and realized gain of the proposed antenna, and (b) Simulated and measured radiation pattern of the proposed antenna.

Table 3.5: Comparing performance with state-of-the-art capsule/Implantable antenna design to the proposed capsule antenna.

Ref.	Size (λ_g^3)	Frequency (GHz)	Physical Dimension (FootPrint) (mm^2)	$\lvert S_{11} \rvert \leq$ -10 dB BW (MHz)	BW (%)	Peak Gain (dBi)	1g-SAR (W/kg)	Implant depth (mm)
[39]	0.16×0.10×0.0008	2.45	20.0×12.3	630	25.7	-30.6	200	NA
[40]	0.13×0.02×0.0005	1.4	27.9×4.3	300	20.8	-26	330	NA
[41]	0.3×0.05×0.001	0.91	98.9×16.5	180	21.6	-19.4	190.5	50
[45]	0.08×0.07×0.002	0.433	55.42×48.5	795	183	-35	225.4	50
[47]	0.24×0.16×0.0004	0.433 /2.4	166.3×110.8	442 /332	102 /23	- 30.64/- 19.86	736 /762	70
[48]	0.03×0.03×0.0003	0.91 /2.45	9.8×9.8	124.7 /154.4	13.6 /6.3	-28.2 / -24.5	420.3 / 233.2	50
[49]	1.01×0.006×0.04	1.4 / 2.45	216.4×8.5	24 / 80	1.71/3.26	NA / NA	NA/NA	12
[52]	0.069×0.069×0.01	2.4 / 4.8	8.5×8.5	85/ 175	3.46/3.64	-26 / - 8.8	207/137	4
[55]	0.2×0.06×0.0016	0.948 /0.951 /1.357	63.3×19	948 /951 /1357	236 /104 /55	-29.71 /-24.9 /-23.2	247 /291 /235	100
This Work	0.14×0.065×0.0006	1.4 / 2.45	30×13.9	500/ 540	35.7/22.0	-22.9 / -25.3	236.0 /139.0	60

3.4 Summary

In this chapter, the presented ingestible wide-bandwidth dual-band antenna emerges as a promising candidate for WCE applications. Its dual-band resonating mechanism has been thoroughly investigated using CMA. Furthermore, the robustness of the dual wide-band antenna impedance characteristic has been rigorously assessed across various implantation scenarios, considering varying implantation depths and distinct capsule thicknesses. The

antenna design offers several advantages, including a compact footprint, an excellent dual wide-band impedance bandwidth, and a nearly isotropic radiation pattern. The measured results confirm the antenna's outstanding performance in both the 1.4 GHz WMTS and 2.45 GHz ISM bands. With impedance bandwidths of 36% and 22% in the respective bands and peak realized gains of -22.9 dBi and -25.3 dBi, it becomes an ideal choice for high-resolution imaging in the gastrointestinal tract. Furthermore, the antenna's low SAR ensures compliance with regulatory requirements for safe human implantation. These findings serve as a foundation for Chapter 4's exploration into enhancing wireless power transfer with Compact and Efficient Dual-Band Rectifiers within WCE systems.